Rowan University

Rowan Digital Works

Shoe–Floor Interactions in Human Walking With Slips: Modeling and Experiments

Mitja Trkov
Rowan University, trkov@rowan.edu

Jingang Yi

Tao Liu

Kang Li

Recommended Citation

Mitja Trkov[1]
Department of Mechanical and
Aerospace Engineering,
Rutgers University,
Piscataway, NJ 08854
e-mail: m.trkov@utah.edu;
mitja.trkov@rutgers.edu

Jingang Yi[2]
Fellow ASME
Department of Mechanical and
Aerospace Engineering,
Rutgers University,
Piscataway, NJ 08854
e-mail: jgyi@rutgers.edu

Tao Liu
School of Mechanical Engineering,
Zhejiang University Hangzhou,
Zhejiang 310027, China
e-mail: liutao@zju.edu.cn

Kang Li
Department of Industrial and
Systems Engineering,
Rutgers University,
Piscataway, NJ 08854
e-mail: kl419@rci.rutgers.edu

Shoe–Floor Interactions in Human Walking With Slips: Modeling and Experiments

Shoe–floor interactions play a crucial role in determining the possibility of potential slip and fall during human walking. Biomechanical and tribological parameters influence the friction characteristics between the shoe sole and the floor and the existing work mainly focus on experimental studies. In this paper, we present modeling, analysis, and experiments to understand slip and force distributions between the shoe sole and floor surface during human walking. We present results for both soft and hard sole material. The computational approaches for slip and friction force distributions are presented using a spring-beam networks model. The model predictions match the experimentally observed sole deformations with large soft sole deformation at the beginning and the end stages of the stance, which indicates the increased risk for slip. The experiments confirm that both the previously reported required coefficient of friction (RCOF) and the deformation measurements in this study can be used to predict slip occurrence. Moreover, the deformation and force distribution results reported in this study provide further understanding and knowledge of slip initiation and termination under various biomechanical conditions. [DOI: 10.1115/1.4038251]

1 Introduction

Occupational slips, trips, and falls are the major cause of workplace injuries [1]. Slips and trips are the most prevalent cause (59%) of falls among elderly [2]. The total cost of the projected falls for year 2020 of the two major groups is over $85 billion [3]. It is therefore crucial to improve the slip prevention methodologies to reduce the number of slips and falls. Slip initiation is governed by the friction characteristics at the shoe–floor interactions. The actual demands of traction between the shoe and floor during walking has been commonly characterized as a measure of required coefficient of friction (RCOF). The RCOF, defined as a ratio of the *total* friction force and the *total* normal force, has been used to determine and predict slips [4–6], and the review of the devices used to measure the shoe–floor friction is discussed in Ref. [7].

Friction characteristics at the shoe–floor interactions involve complex relationships among biomechanical parameters, such as the normal load, shoe angle, sliding speed, as well as the tribological parameters, such as hardness of the shoe sole and roughness of the floor. Among these, the increase of a sliding speed was shown to reduce the coefficient of friction (COF) [8]. In Ref. [9], the effects of the shoe sole hardness on COF were analyzed by comparing the peaks of the RCOF during walking, suggesting that the portion of slips was greater when wearing hard sole shoes than soft sole shoes. Surprisingly, in a later study from the same group [10], it was concluded that the shoe sole hardness does not influence the probability of slip-and-fall events. Similar observation were reported in a recent study [11], showing that the probability of slips was statistically uncorrelated by changing the hardness of the shoe sole material. It is therefore important to further investigate the effect of the biomechanical and tribological parameters on RCOF. The effects of changing the biomechanical parameters

on the measured COF in Ref. [12] suggested that the increased shoe angle decreases the COF. The study, however, did not investigate the effect of parameters such as the shoe–floor pressure distribution on changes of the COF.

Under dry conditions, the roughness of two contact surfaces is one of the most important factors that determine the COF between the shoe sole and floors [13]. A friction and wear model between the shoe and the floor surface was developed in Ref. [14]. The model analyzed dry soft-solid contact considering surface roughnesses and statistical asperity height distribution. A finite element approach in Refs. [15,16] used a simplified macromodel and a realistic shoe–floor model to study their interactions. However, no comparison results are reported with the overall shoe–floor friction tests. Unlike the dry surface contact, the shoe–floor friction is often greatly affected by the presence of the contaminant on the floor that represents a serious slip hazard [1]. In the presence of a liquid contaminant, a pure hydrodynamic lubrication is formed at the shoe–floor interface, or a mixed dry and hydrodynamic lubrication is present. A friction model in Ref. [8] analyzed the mixed-lubrication at the shoe–floor contact interaction.

The soft-solid contact with slip has been analyzed for applications such as tire-road interactions [17] or fingertip grasping [18]. Models for complex soft-solid contact have been successfully demonstrated to capture the friction forces and deformation distributions on the contact patch [17]. Modeling parameters such as the contact area size, the normal load distribution, and the material properties were shown to affect the interaction properties. The purpose of this study is to develop a computational model to capture the complex shoe–floor interactions and to predict slip occurrence. We extend a beam-spring network model in Refs. [17,19] to analyze the shoe–floor interactions. The proposed modeling approach serves as an additional tool that complements the existing experimental studies analyzing the shoe–floor interactions during walking with slips. Comparing to the tire–road interaction [19], the shoe–floor interactions are much more complex due to the irregular contact footprint and pressure distributions. Additional complexity arises from the dynamic, time-varying configurations during walking with slips.
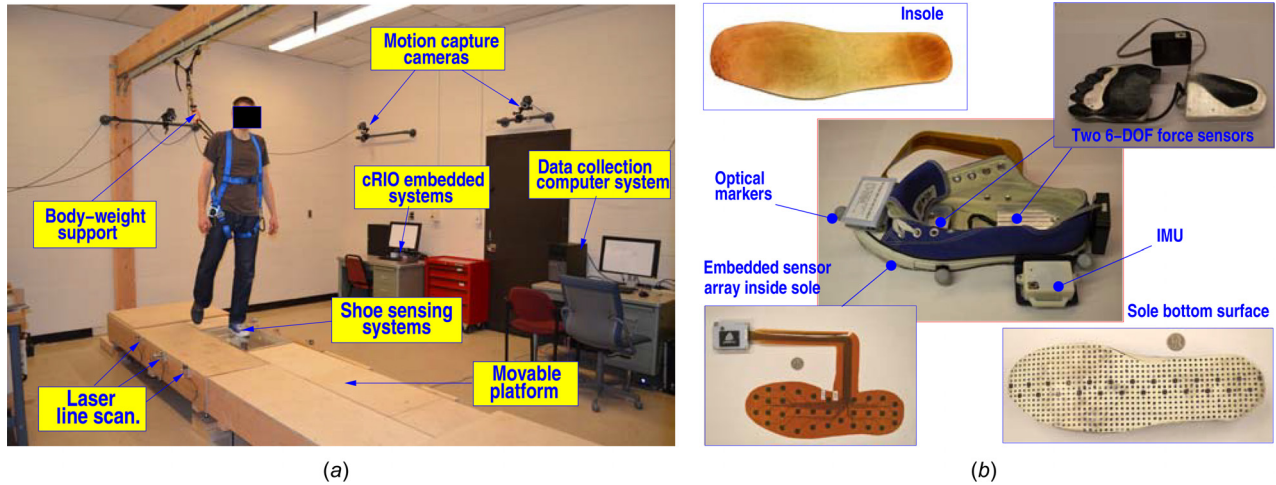
Fig. 1 (*a*) The slip and fall experimental setup with various sensor suites and (*b*) instrumented shoe kinematics/kinetics/forces distribution sensing suite

For the purpose of model validation, we build a shoe–floor sensing suite that integrates pressure–force–kinematics measurements. We used wearable six-degrees-of-freedom (6DOF) force sensors to measure three-dimensional (3D) ground reaction forces (GRF) and torques and a set of two-dimensional pressure sensor arrays are implanted inside the soles [20]. The sole pressure sensors are similar to the pressure-sensitive, electric conductive rubber (PSECR) sensor in Ref. [21].

This paper aims to analyze the complex shoe–floor interactions during walking and slip gaits using a computational modeling approach. Our developed model includes biomechanical and tribological parameters to predict shoe sole deformation distribution and slip initiation. The simulation results were compared to the experimental results to validate the model. We further tested the hypothesis that slip would be terminated sooner if the subject would apply similar normal force profiles as during natural nonslip walking gait. These findings could have practical implications for slip-and-fall prevention. This paper extends the previous conference publication [22] by providing additional experiments, analyses, and discussions. The main contributions of this work are threefold. First, for the first time, this paper discusses the friction force and slip distributions at the shoe–floor interactions during walking with slips. Most existing work use the resultant total friction and normal forces to describe and quantify the slip occurrence, and therefore, the work presented in this paper complements and advances the knowledge of the slip biomechanics. Second, this paper presents a novel, wearable sensing system to capture the foot pressure–force–kinematics interactions. The shoe–floor sensing system in this paper enables further development of wearable, assistive robotic devices for preventing slip-induced falls and potentially other rehabilitation applications. Finally, the developed model can also serve as a potential tool and guidance for improving and designing new shoe soles to enhance the slip-induced fall prevention.

2 Methods

Figure 1 shows the integrated kinematics/kinetics/force sensing suite for the shoe–floor interactions. The sensing suite consists of multiple modality sensory system: (1) the optical markers for indoor motion capture system (8 Bonita cameras, Vicon, Inc., Oxford Metrics, Oxford, UK) and small wireless inertial measurement units (Motion Sense, Inc., Hangzhou, China) to obtain the kinematic information of the foot. The inertial measurement units consists of a triaxial gyroscope, a triaxial accelerometer, and three magnetometers to measure the three attitude angles. (2) Two 6DOF force/torque sensors (model SS-1, INSENCO Co., Ltd., Hangzhou, China) to measure the total 3D forces and torques at

the forefoot and hindfoot contacts. These 6DOF force sensors are thin (12 mm thick for the forefoot sensor and 17 mm thick for the hindfoot sensor) and are embedded inside the shoe under the insoles (Fig. 1). Additionally, we glued a 3D-printed unit (4-mm thickness as shown in Fig. 1(*b*)) under the force sensor to fit the bottom of the barefoot shape. The force and torque measurements are transmitted through wireless Ethernet protocol to the host computer. (3) A PSECR sensor array (of 32 independent sensor units) is embedded inside the sole rubber layer to measure the shoe–floor contact pressure distribution. The PSECR sensors are customly designed and fabricated. These flexible sensors are packaged within a thin-film layer and embedded into two shoe soles with different hardness of the sole material. One array of sensors was molded into a urethane rubber layer (5 mm thick). The thin rubber layer is then glued to the bottom of a regular sport shoe. Another sensor array is glued between a soft rubber (10 mm thick) and the shoe. Each individual flexible force sensor was calibrated by using a computer-controlled linear stage with a 6DOF force/torque sensor (model 45E15 from JR3, Inc., Woodland, CA).

We used a similar setup to measure the coefficients of friction between the shoe sole and the floor under dry and soap contaminated conditions. These parameters (see Table 1) were determined from experimental testing. We mounted the shoe on a dual-axial linear stage to slide the shoe along the acrylic plate. A 25-kg weight was used as the applied normal load, and the shoe was manually pulled using a winch. Normal forces were measured using a 6DOF force/torque sensor (JR3, Inc., Woodland, CA), and friction forces were measured by the S-type load cell (model XTS4, Load Cell Central, Milano, PA). We performed tests under dry and soap-lubricated floor conditions. Lubrication was applied in a same manner as during subject experiments to guarantee similar conditions. The value of the static coefficient of friction was taken as the maximum friction calculation prior to the sliding of the shoe, while the value of the dynamic coefficient of friction was determined as the average friction coefficient during sliding motion.

To measure and calculate the contact contour at the shoe–floor contact, we use six laser line generators and a camera system with image acquisition and processing algorithms. Figure 2(*a*) shows the shoe–floor contact contour measurement system. Six laser line

Table 1 Model parameters for the shoe–floor force models

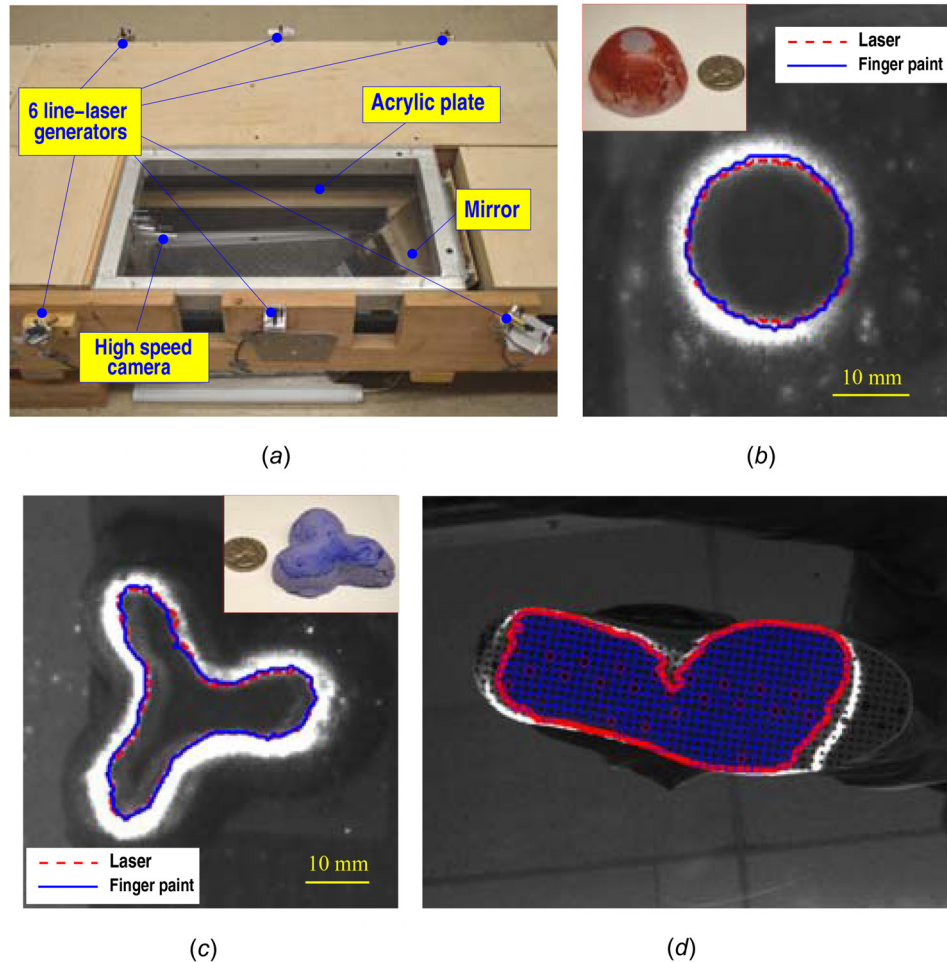| h	μ	σ_{Heel}	μ_{DryStat}	μ_{DryDyn}	μ_{SoapStat}	μ_{SoapDyn}
0.005	0.1	0.4	1.05	0.75	0.55	0.1

Fig. 2 (*a*) Laser-based contour footprint setup. Validation results of laser-based contour measurements by a (*b*) spherical regular object and (*c*) concave irregular object. (*d*) The outcomes of the contact contour, sole surface dots (squares □) and landmarks (diamonds ◇) detection on a snapshot during self-selected walking gait.

generators are placed at various directions to precisely aim at the shoe sole right above the floor surface. These lasers are used to form a closed contour on the sole bottom surface, see Figs. 2(*b*)–2(*d*). A fast-speed camera (Prosilica GX1050C color camera, 1024×1024 pixels, 112 fps) is mounted underneath the transparent acrylic floor surface. The size of the square-imaged area is 350×350 mm and the resolution is 0.3 mm/pixel. The error due to the distortion of the lens is approximately 0.07 mm. To validate the laser-based contour measurements, Figs. 2(*b*) and 2(*c*) show two testing results for a regular shape object (a rubber hemisphere) and an irregular shape object (concave rubber toy), respectively. The comparisons between the laser-based measurements and the surface-paint contour in the figure confirm the nonintrusive approach to accurately obtain the contact contour. Figure 2(*d*) shows a typical laser-based shoe–floor contour measurement during a walking gait with self-selected speed.

In the experiments, we used two types of shoe sole materials: a 10-mm thick soft sole (Neoprene rubber, hardness Shore 30A, McMaster-Carr, Inc., Robbinsville, NJ) and a 5 mm thick hard sole (Polyurethane rubber, hardness Shore 70A, PMC-770, Smooth-On, Inc., Macungie, PA). Selected hardnesses approximately match that of soft sport shoes and heeled working shoes. Each of them was glued to the same type of the sport shoes after we sanded off the threads on the shoes. Using a 3D printer, we fabricated a thin solid layer (thickness of 0.5 mm) with a set of black dots printed on the outer surface and a transparent surrounding material glued to the bottom of the hard sole shoe; see Fig. 1.

Due to the difficulty to match the hardness of the thin printed layer for the soft rubber, we directly painted dots at the bottom of the soft sole. Two types of black dot arrays are used: a set of 3-mm diameter dots are used for calculating the deformation and slip distribution, and a set of 25 dots with a 6 mm diameter are used as the landmarks to localize the smaller dots in the image processing algorithms. To obtain the contact contour and to compute the deformation and slip distributions, we designed and implemented a vision-based processing algorithm similar to the one in Ref. [21]. Figure 2(*d*) shows the detected small dots (square marks □) and landmarks (diamond marks ◇) of a footprint snapshot during human walking gait. The data collection among the optical motion capture, the ground reaction forces and normal force distributions, and the vision-based measurements are synchronized through the analog triggering signal connections among CompactRIO (from National Instruments, Inc., Austin, TX), the Vicon system, and the data acquisition computer. The sampling frequency for all the sensors is 100 Hz.

We conducted human subject testing for both walking and walking with slip gaits. Both types of the experiments were conducted on the walking platform shown in Fig. 1. A healthy young man was recruited to conduct the experiments. The subject's mass and height were 80 kg and 184 cm, respectively. During all tests, the subject wore safety harness attached to the rail on the overhanging beam to ensure safety in case of slip-and-fall. The rope's length was adjusted so that the subject could not touch the floor when in sitting position. The carriage of the rail was manually

pushed to guarantee that the rope was constantly slack during non-slip walking. Such setting allowed unconstrained walking and guaranteed safety of the subject. The subject wore smart shoes sensors and was asked to first walk on the platform with his self-selected walking speed. The walking speed was similar for all three presented gaits (1.3 ± 0.1 m/s). We determined walking speed using the measurements of the motion capture marker mounted on the heel during one gait cycle immediately before the heel strike (HS). The presented plots and results show a representative stance data during each gait. This guarantees precise matching in time among various analyzed parameters during that stance. In the second test, the subject was asked to repeat the test by walking on the platform unaware of the reduced COF at the acrylic plate. To achieve this sudden friction reduction, a cloth was permanently placed on the platform surface at the position of one step ahead of the acrylic plate, and liquid soap was applied in certain experimental runs. The cloth provided enough friction not to cause slip, while the next step on the acrylic plate caused the subject to slip. Soap was manually applied when the subject was facing away from the platform. The subject did not expect slip, and there was no indication of learning or changes in the gait by the subject.

Before conducting any experiments, the subject was informed with the consent form of the testing protocol approved by the Institutional Review Board at Rutgers University. The subject was informed that there is a possibility of foot slippage and fall. Prior to conducting testing, the subject was asked to walk on the platform to become familiar with the testing environment.

3 Shoe–Floor Contact Forces Models

The sole–floor friction forces heavily depend on the normal force distribution between the shoe and the floor. In this section, we present a model to obtain normal load distribution under the shoe using the measurements from the embedded force/torque sensors. We then present a computational scheme for obtaining the friction force distribution.

3.1 Normal Contact Forces Model. Figure 3 illustrates the configuration for the contact forces modeling. The shoe–floor contact patch is denoted as $\mathcal{C}$. A sole–floor contact frame $\mathcal{B}(x, y, z)$ with the origin at the rear tip location C_1 is attached to $\mathcal{C}$ and has its y-axis tangent to $\mathcal{C}$ and the x-axis pointing forward. The x-axis intersects $\mathcal{C}$ at point C_2; see Fig. 3. We denote the left portion $\overset{\frown}{C_1 C_+ C_2}$ of $\mathcal{C}$ as function $y_+(x)$ and right portion $\overset{\frown}{C_1 C_- C_2}$ as function $y_-(x)$. For point $P(x, y)$ on $\mathcal{C}$, we denote the three-directional forces as $f_x(x, y), f_y(x, y)$ and $f_n(x, y)$, respectively.

We take a decomposition approach to obtain the model for $f_n(x, y)$. The form of $f_n(x, y)$ is expressed as the product of the longitudinal normal load $f_{nx}(x)$ and the lateral force factor $f_{ny}(x, y)$. For any $0 \leq x \leq l_s$, $y_-(x) \leq y \leq y_+(x)$, where l_s is the maximum x-coordinate of the front tip point of $\mathcal{C}$, we obtain
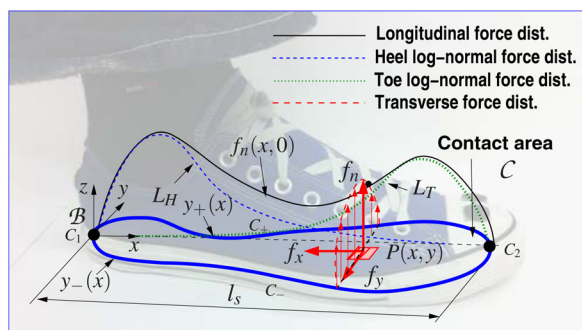
$$f_n(x, y) = f_{nx}(x) f_{ny}(x, y) \quad (1)$$

The form of $f_{nx}(x)$ consists of the contributions from the heel (H) part and the toe (T) part. Both parts are constructed as the sum of two log-normal probability density distribution-like functions, namely

$$f_{nx}(x) = [s_H L_H(x; \mu_H, \sigma_H) + s_T L_T(l_s - x; \mu_T, \sigma_T)]$$

where $L_i(x; \mu_i, \sigma_i) = 1/x_i \sigma_i \sqrt{2\pi} \exp\left(-(\ln x_i - \mu_i)^2/2\sigma_i^2\right), i = H, T$, is the log-normal distribution density function. Coefficients s_H and s_T are the scaling factors for the heel and toe force distributions, respectively.

For a given x, factor $f_{ny}(x, y)$ in Eq. (1) models the normal force distribution on a transverse area $\mathcal{C}_x$, shown as the shaded area in Fig. 4(a). Within $\mathcal{C}_x$, there are n_x PSECR sensor units, denoted as S_j and located at (x, y_{sj}), with normal force measurements as F_{sj}, $j = 1, \ldots, n_x$, respectively. For example, in Fig. 4(a), $n_x = 3$. We denote the boundary points of $\mathcal{C}_x$ with $y_+(x)$ and $y_-(x)$ as C_+ and C_-, respectively. To construct the shape of the actual normal force along the y-axis with finite measurements as shown in Fig. 4(b), we consider $f_{ny}(x, y)$ as a linear combination of a series of Legendre polynomials up to the fifth-order, namely

$$f_{ny}(x, y) = \sum_{i=0}^{5} a_i P_i(u), \ u(y) = -1 + 2 \frac{y(x) - y_-(x)}{y_+(x) - y_-(x)} \quad (2)$$

where a_i are the coefficients that will be determined later in this section, and $P_i(u)$, $u \in [-1, 1]$, are the ith-order Legendre polynomial [23]. The reason to use the fifth-order Legendre polynomials in Eq. (2) is primarily due to its sufficiency to approximate the shape of the normal force. Note that the mapping $y \mapsto u$ changes the variable from $y_-(x) \leq y \leq y_+(x)$ to $-1 \leq u \leq 1$ for a given x. Considering the property of Legendre polynomials, from Eq. (2) we immediately obtain

$$\int_{y_-(x)}^{y_+(x)} f_{ny}(x, y)dy = \frac{y_+(x) - y_-(x)}{2} \int_{-1}^{1} \sum_{i=0}^{5} a_i P_i(u)du = \frac{a_0}{K} \quad (3)$$

where $K = 1/y_+(x) - y_-(x)$.

We construct an algorithm to estimate coefficients a_i, $i = 0$, $\ldots, 5$. As shown in Fig. 4(b), for the given sensor measurements F_{sj}, $j = 1, \ldots, n_x$, we normalize F_{sj}s by the total area S_{C_x} of

Fig. 3 A schematic of the shoe–floor contact and force distributions
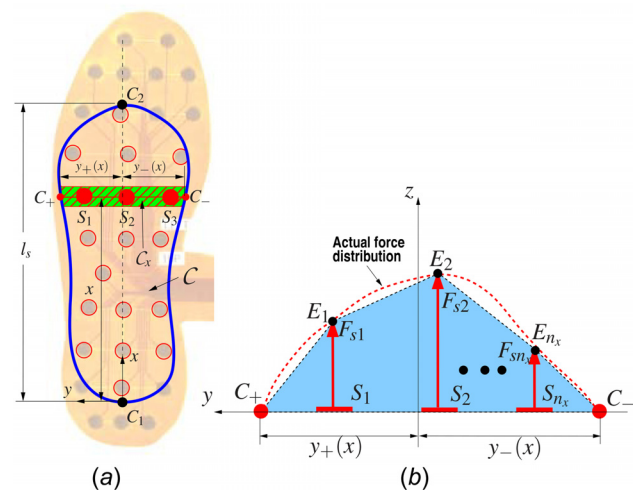

Fig. 4 Schematic of the lateral force distribution calculation: (a) flexible PSECR sensor array and calculation configuration and (b) cross section view of the normal force measurements along section $\mathcal{C}_x$

polygon $C_+E_1E_2E_{n_x}C_-$ and factor K, and then, these normalized forces are equal to the values given by Eq. (2) at (x, y_{sj}), namely

$$f_j = \frac{F_{sj}}{S_{C_x}K} = \sum_{i=0}^{5} a_i P_i(u_j), \quad u_j = u(y_{sj}), \quad j = 1, \ldots, n_x$$

For boundary points C_+ and C_-, the normal forces are both zero and we obtain

$$0 = \sum_{i=0}^{5} a_i P_i(1) = \sum_{i=0}^{5} a_i P_i(-1)$$

Since $f_{ny}(x, y)$ is a normalized force factor, in Eq. (3) we assign $a_0 = 1$ to simplify the calculation. The above relationships for known forces at sensors locations give us a total of $(n_x + 2)$ equations to obtain coefficients a_i, $i = 1, \ldots, 5$. Notice that for the flexible PSECR sensor arrays as shown in Fig. 4(a), $n_x = 1, 2, 3,$ or 4. The estimates of parameters a_i are obtained through a least square method by using the PSECR flexible sensor measurements.

For the longitudinal normal force load parameters μ_i and σ_i, $i = H, T$, the x-coordinates at the maximum normal forces for μ_H (μ_T) and μ_T (μ_H) are satisfied by the relationship, $\mu_H + \mu_T = l_s$. We treat $\sigma_H = \sigma_T$ as a constant during the entire stance and estimate its value by the PSECR sensor measurements. The values for scaling factors s_H and s_T are estimated directly from the heel and toe smart shoe sensor outputs.

The use of the Legendre polynomial-based approximation for $f_{ny}(x, y)$ and the log-normal distribution function for $f_{nx}(x)$ has several advantages. For any given x, the integration of $f_{ny}(x, y)$ over y is always equal to 1 due to the properties of the Legendre polynomials. Therefore, the higher-order Legendre coefficients a_is can be tuned online to capture various transverse pressure distributions for different gait patterns (such as supination or pronation) without changing the total force values. Moreover, the integration of $L_i(x; \mu_i, \sigma_i)$ over a large range of x is also approximated to 1, and thus, the scaling factors s_H and s_T are approximated as the exact normal forces measurements from the smart shoe. Besides a compact form, the log-normal distribution offers the advantage of specifying the location of the peak and the width of the peak for the pressure distribution along the x-axis direction. This property is directly used to tune the model parameters with measurements from the PSECR and smart shoe sensors.

3.2 Contact Friction Forces Model. It is challenging to obtain a closed-form formulation for the shoe–floor friction force and slip distributions; therefore, we instead take a computational approach to obtain them. Similar to the approach described in Ref. [17], a beam-spring network framework is used to compute the local deformation and the friction force distributions simultaneously. Compared to the tire-road model in Ref. [17], the shoe–floor contact area has irregular shape, and the size of the shoe–floor contact is constantly changing with time. Another difference with the tire–road interactions is that the boundary force is no longer distributed across the boundary of the contact patch. Instead, the boundary force is uniformly distributed across the entire contact due to the solid shoe sole configuration.

Figure 5 illustrates the schematic of the beam-spring network model. The contact contour C is partitioned into N virtual cantilever beams and each of them has a height of h (sole layer thickness) and a square cross section with dimension $c \times c$, where c is the side length. Virtual linear springs connect each pair of neighboring beams. We assume that for each beam, elongation and compression are ignored, and only bending deformation is considered.

We assume that the boundary friction force is evenly distributed across the entire contact patch due to the beams being rigidly connected to the top rigid surface. Neglecting the dynamic motions of the beams, for the ith beam, $i = 1, \ldots, N$, the following force balance relationship is obtained:
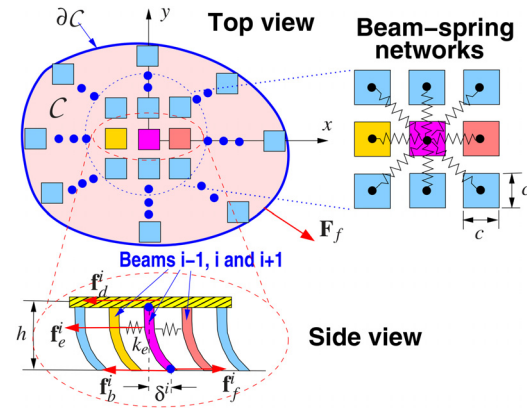

Fig. 5 A schematic of the hybrid beam-spring network model to capture the shoe sole–floor interactions

$$\mathbf{f}_f^i + \mathbf{f}_b^i + \mathbf{f}_e^i + \mathbf{f}_d^i = 0 \tag{4}$$

where $\mathbf{f}_f^i = [f_x^i \; f_y^i]^{\mathrm{T}}$ is the contact friction force, $\mathbf{f}_d^i$ is the evenly distributed boundary friction force applied at the top of all of the beams, $\mathbf{f}_b^i$ is the bending force that captures the shear deformation, and $\mathbf{f}_e^i$ is the resultant net elastic spring force; see Fig. 5. The resultant elastic force $\mathbf{f}_e^i$ and bending force $\mathbf{f}_b^i$ are calculated similarly as in Ref. [17]. The bending force is defined as $\mathbf{f}_b^i = k_b \boldsymbol{\delta}^i$, where $\boldsymbol{\delta}^i = [\delta_x^i \; \delta_y^i]^{\mathrm{T}}$ is the tip deflection vector of the ith beam, and $k_b = 3EI/(h)^3$ is the bending stiffness of the beam.

The Coulomb friction model is adopted to compute $\mathbf{f}_f^i$. If $|\mathbf{f}_b^i + \mathbf{f}_e^i| < \mu f_z^i$, where $f_z^i = f_n^i c^2$ is the normal force at the tip of the ith beam, the beam is stuck and has no movement. In this case, $\mathbf{f}_f^i$ balances the resultant force of $\mathbf{f}_b^i$, $\mathbf{f}_d^i$, and $\mathbf{f}_e^i$. If $|\mathbf{f}_b^i + \mathbf{f}_d^i + \mathbf{f}_e^i| \geq \mu f_z^i$, $|\mathbf{f}_f^i| = \mu f_z^i$ cannot fully sustain the resultant of $\mathbf{f}_b^i$, $\mathbf{f}_d^i$, and $\mathbf{f}_e^i$. The beam will then slip until the force equilibrium holds again at the new location. $\mathbf{f}_b^i$ is assumed to be saturated when the ith beam slips.

With the above formulation, a computational algorithm is used to obtain deformation distribution $\mathbf{u}$ and friction force $\mathbf{f}_f$ on C simultaneously. For completeness of the modeling description, we extend the computational model in Ref. [17] and present Algorithm 1 used in the shoe–floor interactions.

4 Results

4.1 Normal Walking Gait Results. The evolution of the contact footprint during a regular walking gait is shown in Fig. 6. The figure shows a sequence of the contact evolution for the left foot from 10% to 90% of the stance. The stance, denoted as S, is defined as a portion of the gait of a single step from the HS ($S = 0\%$) to the toe-off ($S = 100\%$), determined from the motion capture and image processing data.

To validate the normal force model, we compare the calculated center of pressure (COP) trajectory during the walking gait using measurements from the flexible PSECR arrays and the smart shoe sensors. Figure 7 shows the comparison results for the experiments when the hard sole was used. We omit the results for the soft sole because of only minimal variations. Figures 7(a) and 7(b) demonstrate the x and y positions of the COP as a function of stance S, while Fig. 7(c) shows the x–y trajectories of the COP by measurements from various sensors. To evaluate the influence of the presence of smart shoes sensors on the pressure distribution, we also conduct the comparison experiments by removing the smart shoe sensors and use only the flexible force sensor array. As clearly shown in Fig. 7, the flexible force sensor measurements do not show any significant differences between the experiments

Algorithm 1: Numerical calculation of the shoe–floor friction contact model.

1 Initialize: Set normal force f_z^i and position $\mathbf{u}^i$ for all N beams. Define $\mathbf{A} \in \mathbb{R}^N$ and set $\mathbf{A}(i) = 1$, $\mathbf{F}_f \leftarrow 0$, $\mathbf{f}_b^i \leftarrow 0$, $\mathbf{f}_e^i \leftarrow 0$, $\mathbf{f}_f^i \leftarrow 0$, $i = 1,\ldots,N$;

2 **while** $\mathbf{F}_f < \mathbf{F}_f^{\text{exp}}$ **do**

3 $\quad$ $\mathbf{F}_f \leftarrow \mathbf{F}_f + \Delta \mathbf{F}_f$, $\mathbf{f}_b^i = k_b \boldsymbol{\delta}^i$, $\mathbf{F}_b = \sum_{i=1}^{N} \mathbf{f}_b^i$;

4 $\quad$ $\mathbf{F}_d \leftarrow -\mathbf{F}_f - \mathbf{F}_b$, update $\mathbf{f}_d^i = \mathbf{F}_d / N$;

5 $\quad$ Set iteration error indicator $Err \leftarrow 1$;

6 $\quad$ **while** $Err > E_{\text{thresh}}$ **do**

7 $\quad\quad$ $Err \leftarrow 0$;

8 $\quad\quad$ **for** $i = 1$ to N **do**

9 $\quad\quad\quad$ Find $\mathcal{N}_i$ and update $\mathbf{f}_e^i$;

10 $\quad\quad\quad$ **if** $\mathbf{A}(i) = 1$ **then**

11 $\quad\quad\quad\quad$ **if** $\|\mathbf{f}_e^i + \mathbf{f}_b^i + \mathbf{f}_d^i\| < \mu f_z^i$ **then**
$\quad\quad\quad\quad\quad$ $\mathbf{f}_f^i \leftarrow -\mathbf{f}_e^i - \mathbf{f}_b^i - \mathbf{f}_d^i$, $\Delta \mathbf{u}^i \leftarrow 0$;
$\quad\quad\quad\quad$ **else** $\mathbf{A}(i) \leftarrow 0$, go to Line 8
$\quad\quad\quad\quad$ **end**

12 $\quad\quad\quad$ $\mathbf{f}_f^i \leftarrow \mu f_z^i \dfrac{\mathbf{f}_e^i + \mathbf{f}_b^i + \mathbf{f}_d^i}{\|\mathbf{f}_e^i + \mathbf{f}_b^i + \mathbf{f}_d^i\|}$, $\Delta \mathbf{u}^i \leftarrow \dfrac{\eta(\mathbf{f}_e^i + \mathbf{f}_b^i + \mathbf{f}_d^i - \mathbf{f}_f^i)}{6Eh}$;

13 $\quad\quad\quad$ $\mathbf{u}^i \leftarrow \mathbf{u}^i + \Delta \mathbf{u}^i$, $Err \leftarrow \max(Err, \|\Delta \mathbf{u}^i\|)$

$\quad\quad$ **end**

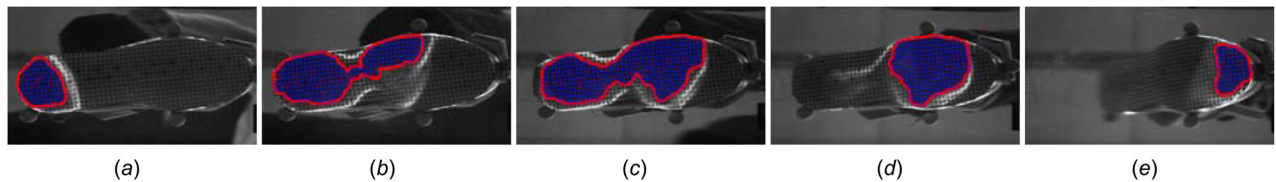$\quad$ **end**

end

Fig. 6 Evolution of the laser-based contact contour and detected dots inside the contour (*a*) 10% of the stance, (*b*) 25% of the stance, (*c*) 50% of the stance, (*d*) 75% of the stance, and (*e*) 90% of the stance during subject's regular walking gait
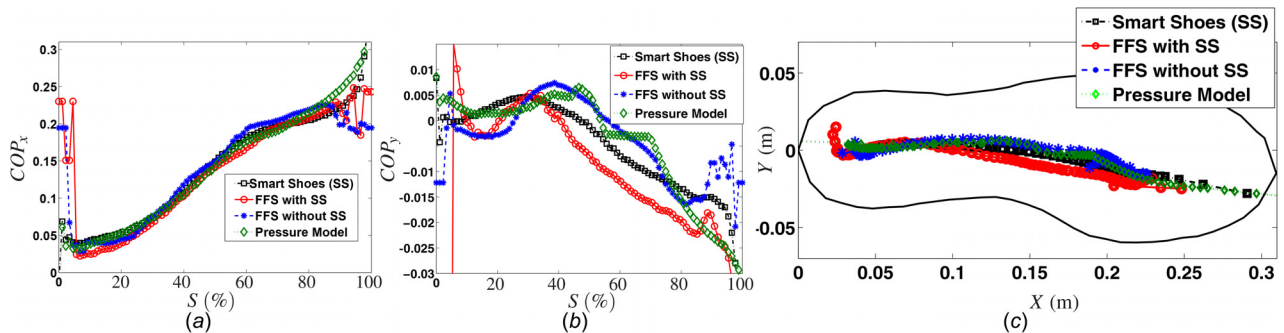

Fig. 7 Comparison results of the COP trajectory during the normal walking gait by various sensor measurements and the normal force model. (*a*) Evolution of the COP in the *x*-axis direction versus the percentage of stance. (*b*) Evolution of the COP in the *y*-axis direction versus the percentage of stance. (*c*) The COP trajectory comparisons in the shoe frame.

with and without wearing the smart shoe sensors. The results also validate that the COP predictions by the proposed normal force model match well with the experiments from both the flexible force sensor array and the smart shoe sensors.

Figures 8(*a*)–8(*c*) show the experimental results of a measured normal load distribution with the hard sole shoes. The results are presented at the beginning ($S = 12\%$), middle ($S = 46\%$), and at the end ($S = 92\%$) of the walking stance, from left to right, respectively. Comparison with the model estimates in Figs. 8(*d*)–8(*f*) demonstrates that the pressure peak locations coincide with those in experiments. The normal load distribution exhibits a single peak at the beginning and end of the stance, and a double peak at the midstance, when the subject shifts weight from the heel to toes.

The measured deformation results of the hard sole are shown in Figs. 8(*g*)–8(*i*). No significant deformations are observed within the contact area. Small deformations occur only at the lowest normal load region, i.e., at the posterior part of the contact area (Fig. 8(*g*)) before contact, and also at the anterior part of the contact area when the foot lifts off the floor (Fig. 8(*i*)). The model predictions show similar deformations (Figs. 8(*j*)–8(*l*)) as those in the experiments. The results for the soft sole in Figs. 8(*m*)–8(*o*) show much larger deformations during walking. The observed deformations are more than one order of magnitude larger compared to those of the hard sole. The largest soft sole deformations are observed at the most posterior section of the shoe at the heel. The deformations at the heel occur at the initial stage of the stance during the heel contact.
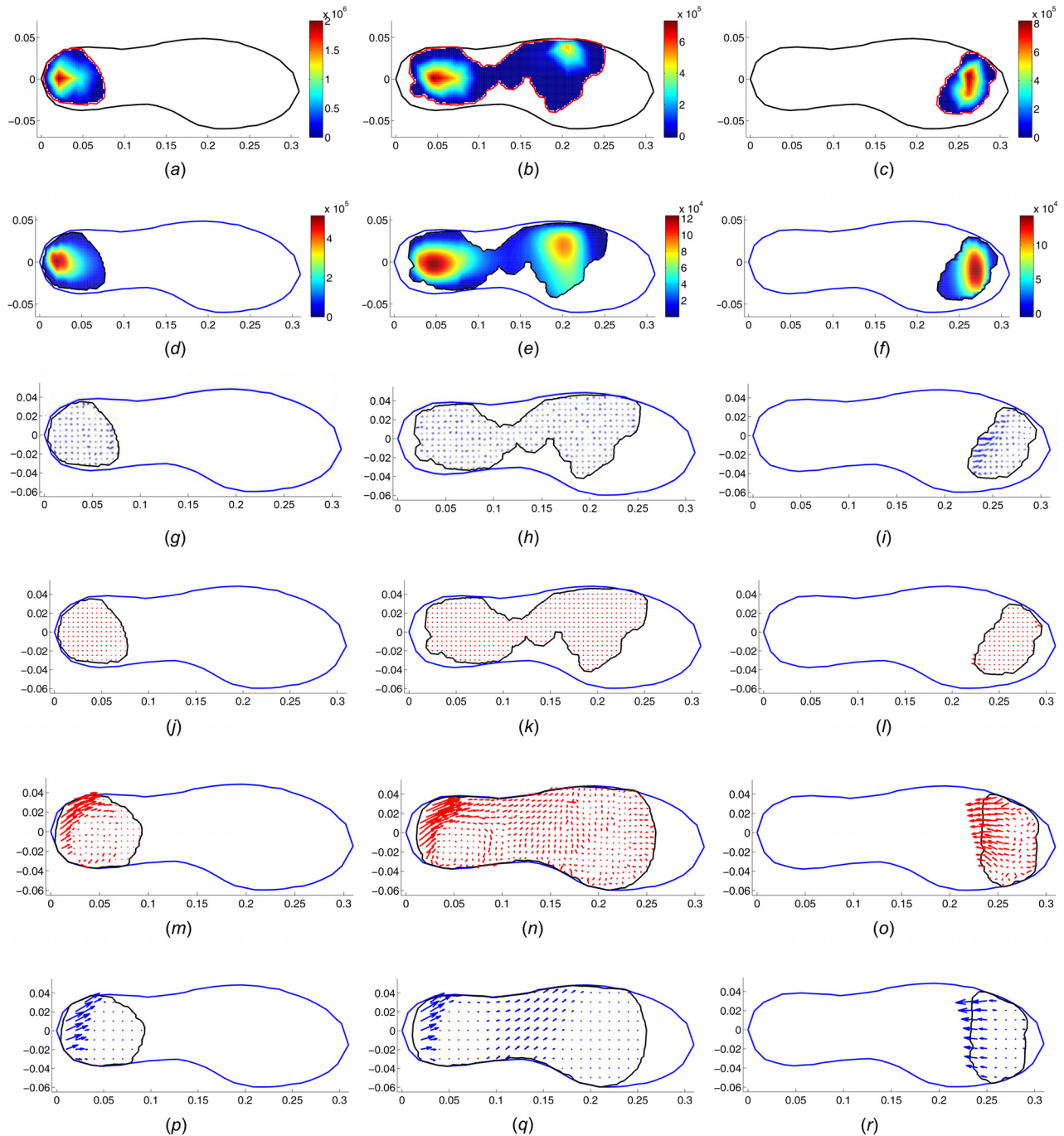
Fig. 8 Experimental (*a*)–(*c*) and simulation (*d*)–(*f*) results of the distributions of the normal load F_n. Experimental (*g*)–(*i*) and simulation (*j*)–(*l*) results of a hard rubber deformations δ magnified by 20×, and experimental (*m*)–(*o*) and simulation (*p*)–(*r*) results of a soft rubber deformations δ magnified by 10×. Results are presented for 12%, 46%, and 92% of stance (*S*). Units of the normal load distributions are N/mm².

The entire flat part of the sole is in contact with the floor at approximately $S = 25\%$. At the midstance, the contact contour and contact area remain almost constant. The largest soft sole deformations occur at the back of the shoe and are mainly due to the large residual deformations generated during the initial contact. Contrary to the hard sole, the soft sole deformations occur even at the center of the contact (i.e., at midfoot), due to the low normal load at that location. At the end of the stance, during the heel-off phase, the shoe is rolling over the front curved portion. Heel part of the shoe starts to move up and forward affecting the sole deformations during the forefoot contact. Large soft sole deformations

are observed at the posterior part of $\mathcal{C}$ during the push-off, while friction force reaches positive peak values.

The contact model successfully predicts the soft and hard shoe sole deformations as observed in the experiments. During normal walking, the sole shows no local deformations or local slip, and thus, no global slip occurs. Figure 9(*a*) shows the values of the RCOF calculated from the smart shoe sensors. The measured COF under various conditions are listed in Table 1. The results in Fig. 9(*a*) confirm that no global slip happens because the measured dry shoe sole–floor coefficient of friction ($\mu_{\text{DryStat}} = 1.05$ in Table 1) is larger than the RCOF.
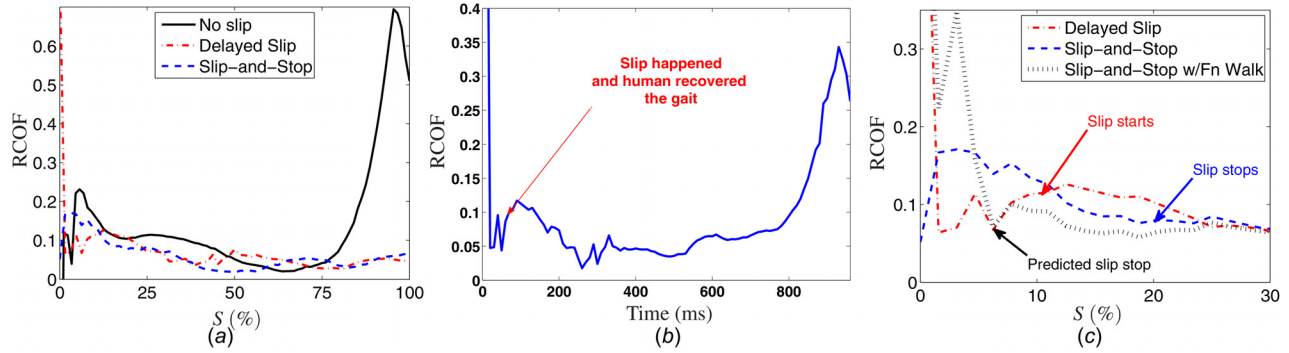
Fig. 9 (a) RCOF from the smart shoe sensors versus the stance for normal walking, delayed-slip and slip-and-stop gaits. (b) ROCF for the delayed-slip over the whole step. (c) Comparison of the RCOF for the delayed-slip, slip-and-stop and the estimated RCOF for the slip-and-stop gait if using the values of the normal force from nonslip walking gait. Marked are instances of the slip initiation for the delayed-slip gait and the slip termination during the slip-and-stop gait.
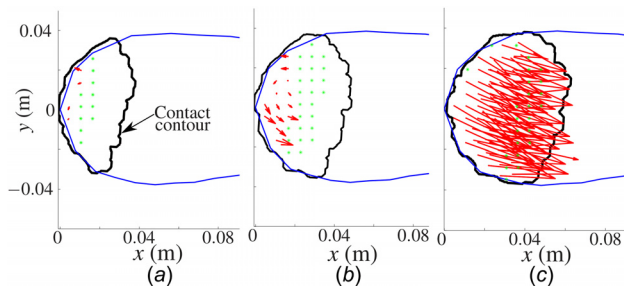

Fig. 10 Measured deformations at (a) 50 ms and (b) 60 ms from the beginning of stance, until slip happens at (c) 70 ms after initial contact. All deformations are magnified by 20 times.

4.2 Foot-Slip Walking Gait Results. Foot slip was induced at the beginning of the stance. Two types of foot slip were observed: "delayed-slip" gait, namely, slip initiated shortly after the heel strike, and "slip-and-stop" gait, that is, slip starts immediately after HS and then comes to a stop after sliding for a short period.

Figure 10 shows the results of the measured deformation from the delayed-slip gait. The initial slip starts at approximately $S = 8\%$ of stance, and it is observed that the dots at the rear portion have almost no deformation compared to the dots at the front edge of the contact contour; see Fig. 10(a). Similar behavior is observed during walking without slip. Gradually, the rear portion starts to slip (Fig. 10(b)), and finally, at around 70 ms after HS, an instantaneous slip occurs over the entire contact area as shown in Fig. 10(c).

Figure 9(b) shows the calculated RCOF as a function of time. We use time plot for comparison rather than stance plot because of the longer duration of delayed-slip gait compared to the normal walking stance. Clearly, at the instance of 70 ms, the slip occurs, and the RCOF is around the available coefficient of friction (ACOF) ($\mu_{\text{SoapDyn}} = 0.1$ in Table 1) for the wet soap condition on the floor surface.

We compute the sole deformation and sole–floor friction distributions before (Figs. 11(a)–11(d)) and after (Fig. 11(e)–11(h))
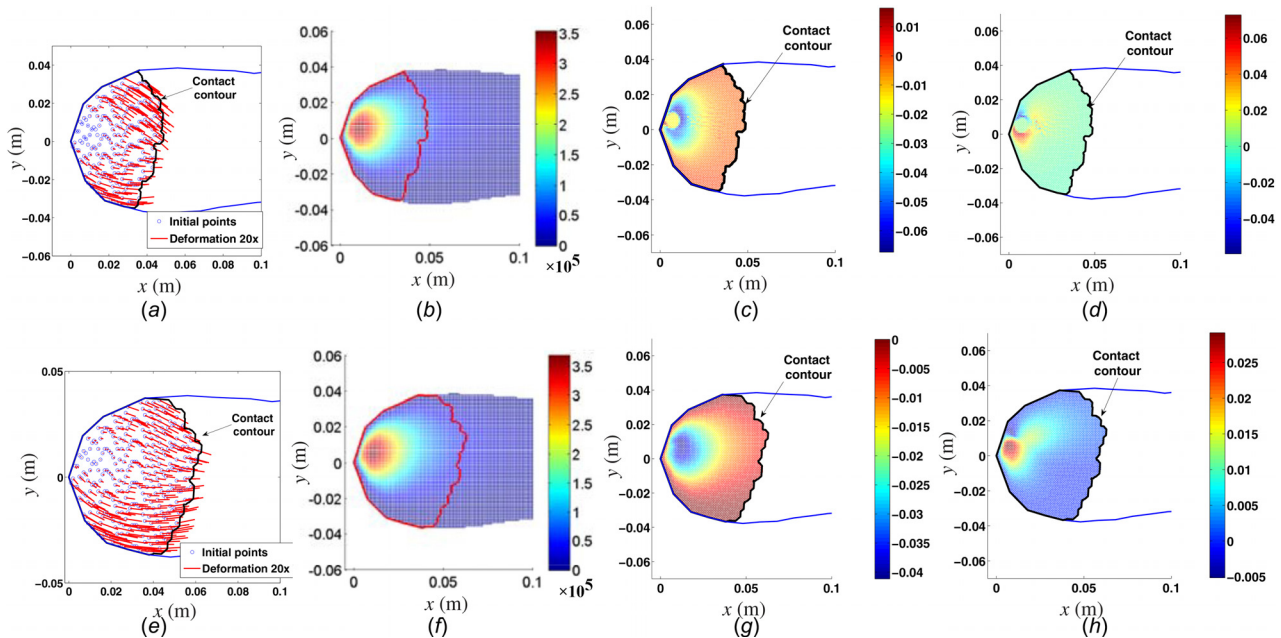

Fig. 11 Results right before slip occurs: (a) computed deformation distribution, (b) measured normal load $f_n(x, y)$, (c) computed longitudinal friction force distribution $f_x(x, y)$, and (d) computed lateral friction force distribution $f_y(x, y)$. Results right after slip occurs: (e) computed deformation distribution, (f) measured normal load $f_n(x, y)$, (g) computed longitudinal friction force distribution $f_x(x, y)$, and (h) computed lateral friction force distribution $f_y(x, y)$. The unit for force distributions is N/mm^2.
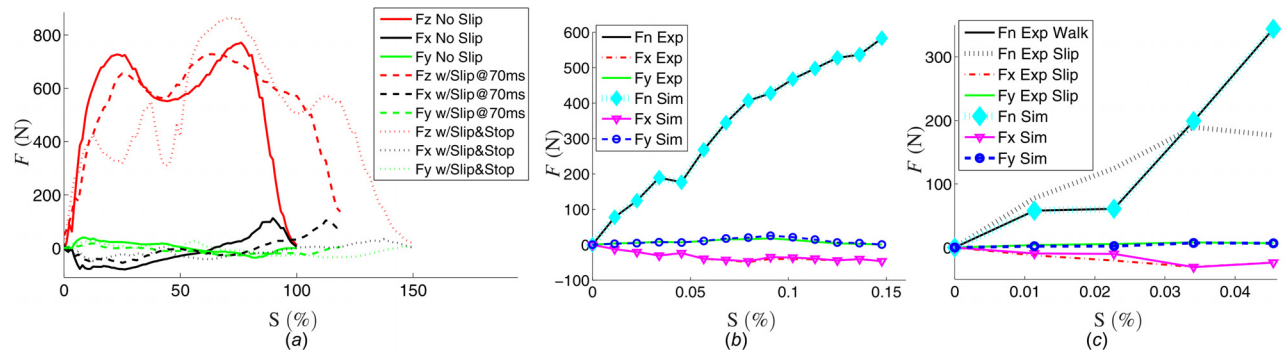
Fig. 12 (*a*) Forces during regular walking gait and walking with foot slip gait plotted with respect to the regular walking stance (*S*). GRFs from the experiments and model predictions for (*b*) regular no slip walking and (*c*) slip-and-stop walking gaits. The curves of "Fn Exp" and "Fn Sim" coincide with each other since we intentionally use the normal forces measured in experiments in the computation.

slip happens. The results demonstrate that the large deformations and slip start at the front edge of the contact area, similar to the observed experimental results. The areas with large normal load slip last. The computed longitudinal and lateral friction force distributions are shown in Figs. 11(*c*) and 11(*d*) (before slip), and Figs. 11(*g*) and 11(*h*) (slip occurred), respectively. We also plot the measured normal force distributions before and after slip as shown in Figs. 11(*b*) and 11(*f*), respectively. At the time instance right before slip, the friction forces have the highest values in the neighborhood around the stick portion of the contact area. The lateral friction force distribution shows the large values but with different signs around the stick contact area (Fig. 11(*d*)). The opposite signs indicate compression and tension in these areas. Friction forces show a smaller value inside the stick region than those in its neighborhood areas. At the instance of slip, both the longitudinal and lateral forces show a high correlation with the normal load distribution and have peak values at the same areas.

Figure 12 shows the *total* normal forces F_n, and *total* longitudinal (F_x) and lateral (F_y) friction forces for three different gaits: normal walking gait, delayed-slip gait, and slip-and-stop gait. The slip results are plotted with respect to the normal walking stance for the step immediately prior to foot slip onset to exclude the effect of the walking speed variations among the tests. Compared to the no-slip walking, the normal forces decrease shortly after the heel strike. Figure 12(*b*) further shows the matched experimental and simulated *total* normal and friction force profiles. Figure 12(*c*) shows the experimental results of the total GRF profiles during the slip-and-stop gait, and the simulation results using the normal force profile from regular walking gait without slip.

Figure 9(*c*) shows the comparison of the RCOF for the three aforementioned gaits. During the delayed-slip gait, the foot slip occurs at 70 ms after the heel strike (at approximately 10% of stance) and ends at approximately 45% of stance (not shown), when the RCOF is already much lower than the ACOF. During the initial portion of slip, the measured RCOF during this initial period is assumed to correspond to the maximum ACOF during sliding. The ACOF is nonconstant, condition dependent, and the conditions such as the normal force, heel velocity, and shoe–floor angle affect the shoe–floor contaminant friction [15]. Although the RCOF is often used for slip prediction, due to changing ACOF, this method cannot be directly used to predict slip termination. Instead, using the proposed friction model we are able to predict slip initiation and termination as shown in Fig. 9(*c*). This offers an important advantage over slip prediction by only RCOF.

During slip-and-stop gait, the foot is slipping from the initial heel contact and stops after 130 ms (at approximated $S = 20\%$). Figure 9(*c*) shows the RCOF changes with stance. When the RCOF values drop below the predicted ACOF, the actual slipping motion did not stop slip termination. Figure 9(*c*) also includes the computed RCOF for such slip-and-stop simulation with the

modified normal force profile. The friction force is kept the same as in slip experiments. Computed RCOF at 40 ms (i.e., $S = 7\%$) after heel strike drops below the ACOF, indicating the potential for earlier slip termination as predicted by the friction model. Compared to the experimental data of the slip-and-stop event, the model with the modified normal force profile predicted that slip stops 90 ms earlier.

5 Discussions

This study aims at understanding and prediction of slip initiation under a hard and soft shoe sole by measuring the sole deformations. The presented results were in agreement with the previously reported conclusion by using RCOF as the slip prediction parameter. The experiments suggested that partial slip was initiated first at the sole–floor contact area with large deformations. Further evolution of slip from these areas can potentially lead to a global slip and therefore, it is important to analyze slip evolution for applications, such as shoe tread design. In the following, we further discuss the model development, explanation, and interpretation of the presented results.

One attractive property of the log-normal distribution function lies in its simplistic form with only two parameters (μ and σ) to characterize the shoe–floor pressure distribution. Model parameter μ (i.e., the median of the distribution) progresses forward similarly as the center of pressure, and therefore, can be interpreted and correlated with biomechanical variables. Parameter σ (i.e., standard deviation) defines the skewness of the distribution function. In this study, the value of parameter σ was much smaller than that of μ. This implies that the mean, median, and mode of the distribution function lie closely together and consequently further supports the previously mentioned correlation between μ and the COP. We considered σ as a tuning parameter to approximately match the shape of the distribution and its peak value. Parameter σ was chosen as a constant over one stance for model simplicity, and its value was estimated through experimental COP measurements.

Moreover, superimposing two log-normal distribution functions in the opposite directions (with individual scaling factor S) allows to generate a double-peak distribution (i.e., under heel and toes). This property is particularly attractive to model and reflect the actual double-peak pressure distribution as observed in experiments. Superposition of two individual functions has an advantage over using a single double-peak function since the former allows greater model flexibility than the latter. It is convenient in our study to use the superposition of two log-normal functions, because two smart-shoe sensors were separately used to measure forces under the heel and the toes, and their measurements can be used to directly tune scaling factors S for both functions.

The Legendre polynomial was used in the normal force model mainly because of its properties to allow lateral variations without affecting the magnitude of the total force. This is attractive for separately determining and tuning the anterior–posterior and medio-lateral pressure functions for a given total normal force. Besides the previously discussed reasons, we used Legendre polynomials in this study because the model also matched the experimental results. It might be possible to find other sets of mathematical functions to model pressure distributions.

We used and recruited only one young healthy male in this study because the focus of our study lies in understanding slip initiation and prediction under normal walking gait. Our goal was to directly compare walking gaits with and without slip. We consider that typical experiments by one healthy subject are sufficient to meet the previously mentioned goal. The presented modeling approach can be applied to other subjects with normal gaits. The friction and normal force models are not restrictive and can be tuned to obtain the model parameters of subjects with abnormal gaits. In such case, the model parameters need to be adjusted to reflect the changes in normal load distribution. Noticing that slip initiation in this study happens at the beginning of the stance when variations of normal load distributions are small, the presented normal load model is still valid and applies to a large population. Of course, we need to further validate the models using multiple subjects before they can be used among all populations. This is one limitation of the work presented in this paper.

For the experimental results, such as gait parameter profiles in Fig. 7(c), we omitted data for the first and last 5% of the stance due to inaccuracy of pressure sensor measurements when the foot contacts and leaves the floor. Results of the COP profiles in Fig. 7 imply that the use of the force sensors inside the shoes does not change the normal gait pressure distribution. The differences of the COP positions in the y-axis direction (Fig. 7(b)) among various sensor measurements could possibly be due to the nonperfect foot-insert that was placed under the smart shoe sensors to emulate the anatomy of the foot and due to the decreased sensitivity of some flexible force sensors at certain locations. Further comparison of the pressure distribution results in Figs. 8(a)–8(f) confirms that the normal load model distribution matches the experimentally observed pressure distribution, and this validates the normal force model. Additionally, the comparison results of the experimental and the model prediction in Figs. 8(g)–8(r) show that the contact model successfully predicts the sole deformations, and this validates the friction force model.

As shown in Fig. 8, although the normal contact force model has successfully predicted the peak locations as observed in the experimental results, the values from the model are smaller compared to the experimental results. This is mainly due to two factors: (1) measurements of the pressure distribution are only at certain locations, and the values at other locations are obtained by linearly interpolation, and (2) limited model capabilities of one lateral distribution function, where the use of Legendre polynomials does not allow generating extremely sharp peaks. Additionally, observations from the simulation results of the friction force distribution right before slip (see Figs. 11(c) and 11(d)) suggest that smaller values occurred inside the stick region compared to those in its neighborhood areas. This could be due to the large contribution of elastic forces in the nonstick areas and also possibly due to the use of Coulomb friction law in the computational model.

During normal walking, the beginning and end of stance are the most crucial phases at which slip likely occurs for several reasons: (1) stick areas at the beginning (Fig. 8(m)) and end of stance (Fig. 8(o)) are both relatively small; (2) the friction forces reach their peak values due to heel-strike and push-off; (3) the newly established contact during heel strike is evolving and does not sustain much normal load yet; and (4) the anterior portions of contacts in both phases have a local slip. The slip experiments presented in the Results section confirm such observation. Another observation is that at the beginning and at the end of the stance, the shoe is often rotated around the z-axis, and the deformations indicating this are shown in Fig. 8(m)). This rotational effect, due to the moment around the z-axis was not considered in our model.

Due to small contact area and the high stiffness of the hard shoe sole material, the hard sole–floor interaction acts like a rigid contact, and thus, the resultant RCOF calculation seems to serve as a good prediction of slip occurrence. However, the sole deformation measurements could serve as a good indicator for possible slip, especially when the actual coefficient of friction is either unknown or is it difficult to obtain it in real time. Using sole deformation as a slip predictor complements the previously reported and well-known slip prediction indicator parameter (i.e., RCOF) and could be used as a true assessment for slip occurrence. Furthermore, the results in Fig. 9(c) also indicate that the RCOF cannot be used to precisely predict slip termination since during slip progression the RCOF values dropped below the ACOF values, while the actual slipping motion did not stop. One advantage of using deformations measurements as the slip indicator is that no prior knowledge of the true sole-floor coefficient of friction is needed. Of course, obtaining the deformation distribution in real time is not straightforward and this is one task among our future research directions. Additionally, we also conducted slip experiments using a soft shoe sole to investigate if any partial slips occur prior to global slip. Unfortunately, our attempt was not successful, due to the extremely low COF (around 0.05) that constantly caused immediate slip and deformation measurements could not be obtained.

Comparing with normal walking, reduction of normal forces during slip gaits was reported as the most significant change among biomechanical variables [24]. Results in Fig. 12(b) confirm such observations. Compared to noslip walking, the normal force during slip decreases shortly after the heel strike, which was reported to be due to the foot slip and not human postural response [24]. The reason for slip biomechanics solely influencing the decrease of normal load is primarily due to the fact that during the initial portion of slip, the subject's postural response is not present yet since the voluntarily response starts after approximately 200 ms [25]. Since the friction force is highly related to the normal force, the reduction of the normal force results in a reduction of friction force and thus increases the possibility of slip initiation. This effect also reduces the possibilities of slip termination. Therefore, we hypothesize that if the subject could voluntarily, or using external assistance, try to restore the normal force profile during slip gait, slip would stop sooner. We validated this hypothesis using the friction model with the normal force profile and distribution from normal walking. We applied these profiles to the slip-and-stop case and kept the other parameters unchanged. The reason for applying this to the slip-and-stop rather than the delayed-slip gaits is to reduce the effects of other biomechanical parameters such as shoe angle, contact area size, etc. that are similar to those in regular walking. These simulation results imply that intentionally trying to keep similar walking gait and normal force profile during slip can lead to terminate slipping sooner. This observation can potentially provide novel slip balance recovery strategies and be beneficial in practical applications of slip-and-fall prevention.

6 Conclusion

We presented modeling, analysis, and experiments of the shoe–floor interactions during human walking with slips. We developed a flexible force and sensing system to measure plantar pressure distribution inside shoe soles. Resultant shoe–floor forces were also obtained by using two 6DOF load-cells under the hindfoot and forefoot. A normal force distribution model was developed and used in the computation of the deformation and friction force distributions of the soft and hard shoe soles with an extended computational friction model. The model revealed the initiation and evolution of the shoe–floor slip and also the friction force distributions. We experimentally validated the normal force

distribution model. The experimental and computational results confirmed that the largest deformations occurred in the areas with the smallest normal load and also that partial slips happened first at the same locations. The comparison results showed a good agreement for the soft and hard sole-floor contacts. One advantage of using the deformation over the RCOF to predict slip occurrence is the qualitative assessment of slip, especially when the friction coefficient is unknown. We plan to conduct experimental verification of the friction force model. Combining the shoe–floor interactions model in this paper with the bipedal dynamics (e.g., Ref. [26]) to study the walking stability under slip is also among our future research tasks.

References

[1] Chang, W.-R., Leclercq, S., Lockhart, T. E., and Haslam, R., 2016, "State of Science: Occupational Slips, Trips and Falls on the Same Level," Ergonomics, **59**(7), pp. 1–23.

[2] Berg, W. P., Alessio, H. M., Mills, E. M., and Tong, C., 1997, "Circumstances and Consequences of Falls in Independent Community-Dwelling Older Adults," Age Ageing, **26**(4), pp. 261–268.

[3] Englander, F., Hodson, T. J., and Terregrossa, R. A., 1996, "Economic Dimensions of Slip and Fall Injuries," J. Forensic Sci., **41**(5), pp. 733–746.

[4] Redfern, M. S., Cham, R., Gielo-Perczak, K., Grönqvist, R., Hirvonen, M., Lanshammar, H., Pai, C. Y.-C., and Power, C., 2001, "Biomechanics of Slips," Ergonomics, **44**(13), pp. 1138–1166.

[5] Chang, W.-R., Grönqvist, R., Leclercq, S., Myung, R., Makkonen, L., Strandberg, L., Brungraber, R. J., Mattke, U., and Thorpe, S. C., 2001, "The Role of Friction in the Measurement of Slipperness—Part 1: Friction Mechanisms and Definition of Test Conditions," Ergonomics, **44**(13), pp. 1217–1232.

[6] Chang, W.-R., Chang, C.-C., and Matz, S., 2011, "The Effect of Transverse Shear Force on the Required Coefficient of Friction for Level Walking," Human Factors, **53**(5), pp. 461–473.

[7] Chang, W.-R., Grönqvist, R., Leclercq, S., Brungraber, R. J., Mattke, U., Strandberg, L., Thorpe, S. C., Myung, R., Makkonen, L., and Courtney, T. K., 2001, "The Role of Friction in the Measurement of Slipperness—Part 2: Survey of Friction Measurement Devices," Ergonomics, **44**(13), pp. 1233–1261.

[8] Beschorner, K., Lovell, M., Higgs, C. F., III, and Redfern, M. S., 2009, "Modeling Mixed-Lubrication of a Shoe-Floor Interface Applied to a Pin-on-Disk Apparatus," Trib. Trans., **52**(4), pp. 560–568.

[9] Tsai, Y.-J., and Powers, C. M., 2008, "The Influence of Footwear Sole Hardness on Slip Initiation in Young Adults," J. Forensic Sci., **53**(4), pp. 884–888.

[10] Tsai, Y.-J., and Powers, C. M., 2013, "The Influence of Footwear Sole Hardness on Slip Characteristics and Slip-Induced Falls in Young Adults," J. Forensic Sci., **58**(1), pp. 46–50.

[11] Beschorner, K. E., Albert, D. L., and Redfern, M. S., 2016, "Required Coefficient of Friction During Level Walking Is Predictive of Slipping," Gait Posture, **48**, pp. 256–260.

[12] Beschorner, K. E., Redfern, M. S., Porter, W. L., and Debski, R. E., 2007, "Effects of Slip Testing Parameters on Measured Coefficient of Friction," Appl. Ergonomics, **38**(6), pp. 773–780.

[13] Chang, W.-R., Kim, I., Manning, D., and Bunterngchit, Y., 2001, "The Role of Surface Roughness in the Measurement of Slipperiness," Ergonomics, **44**(13), pp. 1200–1216.

[14] Kim, I.-J., and Nagata, H., 2008, "Research on Slip Resistance Measurements—A New Challenge," Ind. Health, **46**(1), pp. 66–76.

[15] Beschorner, K. E., 2008, "Development of a Computational Model for Shoe-Floor-Contaminant Friction," Ph.D. thesis, University of Pittsburgh, Pittsburgh, PA.

[16] Moghaddam, S. R. M., Redfern, M. S., and Beschorner, K. E., 2015, "A Microscopic Finite Element Model of Shoe-Floor Hysteresis and Adhesion Friction," Tribol. Lett., **59**(42), pp. 1–10.

[17] Zhang, Y., and Yi, J., 2014, "Static Tire/Road Stick-Slip Interactions: Analysis and Experiments," IEEE/ASME Trans. Mechatronics, **19**(6), pp. 1940–1950.

[18] Ho, V.-A., Dao, D. V., and Hirai, S., 2011, "Development and Analysis of a Sliding Tactile Soft Fingertip Embedded With a Microforce/Moment Sensor," IEEE Trans. Rob., **27**(3), pp. 411–424.

[19] Zhang, Y., and Yi, J., 2012, "Tire/Road Stick-Slip Interactions: Analysis and Experiments," ASME Paper No. DSCC2012-MOVIC2012-8619.

[20] Liu, T., Inoue, Y., Shibata, K., and Shiojima, K., 2012, "A Mobile Force Plate and Three-Dimensional Motion Analysis System for Three-Dimensional Gait Assessment," IEEE Sens. J., **12**(5), pp. 1461–1467.

[21] Zhang, Y., Yi, J., and Liu, T., 2013, "An Embedded Local Force Sensor for In-Situ Tire-Road Interaction Measurements," IEEE Sens. J., **13**(5), pp. 1756–1765.

[22] Trkov, M., Yi, J., Liu, T., and Li, K., 2014, "Shoe-Floor Interactions During Human Slip and Fall: Modeling and Experiments," ASME Paper No. DSCC2014-6184.

[23] Abramowitz, M., and Stegun, I. A., 1964, Handbook of Mathematical Functions: With Formulas, Graphs, and Mathematical Tables, Dover Publications, Mineola, NY.

[24] Beschorner, K. E., and Redfern, M. S., and Cham, R., 2013, "Earliest Gait Deviations During Slips: Implications for Recovery," IIE Trans. Occup. Ergon. Hum. Factors, **1**(1), pp. 31–37.

[25] Patla, A. E., 2003, "Strategies for Dynamic Stability During Adaptive Human Locomotion," IEEE Eng. Med. Biol. Mag., **22**(2), pp. 48–52.

[26] Chen, K., Trkov, M., Yi, J., Zhang, Y., Liu, T., and Song, D., 2015, "A Robotic Bipedal Model for Human Walking With Slips," IEEE International Conference on Robotics and Automation (ICRA), Seattle, WA, May 26–30, pp. 6301–6306.